



One-step hydrothermal fabrication of visible-light-responsive AgInS₂/SnIn₄S₈ heterojunction for highly-efficient photocatalytic treatment of organic pollutants and real pharmaceutical industry wastewater



Fang Deng^a, Fei Zhong^a, Decai Lin^a, Lina Zhao^a, Yuejing Liu^a, Jinhong Huang^a, Xubiao Luo^{a,*}, Shenglian Luo^{a,*}, Dionysios D. Dionysiou^b

^a Key Laboratory of Jiangxi Province for Persistent Pollutants Control and Resources Recycle, Nanchang Hangkong University, Nanchang 330063, PR China

^b Environmental Engineering and Science Program, Department of Biomedical, Chemical and Environmental Engineering (DBCEE), University of Cincinnati, Cincinnati, OH, 45221-0012, USA

ARTICLE INFO

Article history:

Received 22 May 2017

Received in revised form 13 July 2017

Accepted 19 July 2017

Available online 20 July 2017

Keywords:

AgInS₂/SnIn₄S₈

Heterojunction

Visible-light photocatalysis

Pharmaceutical industry wastewater

Mineralization

ABSTRACT

Although ternary chalcogenide compounds are effective photocatalysts for degrading organic pollutants under visible-light irradiation, their photocatalytic activity and stability are still low and far from practical application. In this study, two-dimensional AgInS₂/SnIn₄S₈ nanosheet heterojunctions were fabricated by one-step hydrothermal method. AgInS₂/SnIn₄S₈ nanosheet heterojunctions have strong visible-light absorption and narrow band gap of 2.27–2.35 eV, and exhibit excellent visible-light photocatalytic activity in the degradation of 2-nitrophenol (2NP) and tetracycline hydrochloride (TC-HCl) compared with pure AgInS₂ and pure SnIn₄S₈, which is attributed to the efficient separation of photogenerated electrons and holes. The practical application of AgInS₂/SnIn₄S₈ nanosheet heterojunctions was further studied. 20 mg AgInS₂/SnIn₄S₈ heterojunctions can effectively treat 100 mL real pharmaceutical industry wastewater in presence of H₂O₂ with 65.98% mineralization efficiency, and the chemical oxygen demand (COD) of pharmaceutical industry wastewater decreases to 153 mg/L, which meets the discharge standards of industrial effluent. Moreover, AgInS₂/SnIn₄S₈ heterojunctions can maintain long-term activity without obvious inactivation after five consecutive catalytic cycles without using regeneration means.

© 2017 Published by Elsevier B.V.

1. Introduction

The discharge of undisposed wastewater has caused many environmental problems [1–3]. Semiconductor photocatalytic degradation has been regarded as a green and sustainable technology in wastewater treatment [4–7]. However, the photocatalytic degradation technology based on traditional catalysts such as TiO₂ cannot effectively degrade organic pollutants under visible-light irradiation due to wide band gap, low charge separation efficiency and poor utilization of solar energy [8–12]. Therefore, the construction of high-efficiently visible-light-responsive photocatalysts is essential [13–15].

Ternary chalcogenide compounds have attracted increasing concern due to their strong visible-light absorption and nar-

row band gap, and have potential application in heterogeneous photocatalysis [16–19]. SnIn₄S₈ (abbreviated as SIS) and AgInS₂ (abbreviated as AIS) are representative ternary chalcogenide materials, and many studies were focused on their visible-light-driven photocatalytic activity for the degradation of organic pollutants [20–22]. Unfortunately, for a single semiconductor, the fast recombination of photogenerated electrons and holes usually results in an unsatisfactory photocatalytic performance [23,24].

Constructing heterojunction photocatalysts with matching band potentials is an effective strategy to accelerate the interfacial charge transfer and decrease the recombination of photoinduced electron-hole pairs, leading to enhanced photocatalytic performance [25–27]. Certainly, some efforts have been made to enhance the photocatalytic activity of AgIn₅S₈ and AgInS₂ by constructing heterojunction photocatalysts with other semiconductors, such as AgIn₅S₈/TiO₂, AgInS₂/TiO₂ heterojunction. The AgIn₅S₈/TiO₂ composite photocatalysts with matched band potentials showed superior visible-light photocatalytic activity for the

* Corresponding authors.

E-mail addresses: luoxubiao@126.com (X. Luo), sllou@hnu.edu.cn (S. Luo).

reduction of aqueous Cr(VI) and H₂ production, and the corresponding H₂ production rate was about 7.7 times higher than that of pure AgIn₅S₈ [28,29]. Liu et al. reported that the TiO₂ and AgInS₂ heterostructures with different mole ratios exhibited substantially improved visible-light photocatalytic degradation of gaseous o-dichlorobenzene [30]. Despite there are tremendous progress on ternary chalcogenides heterojunction photocatalysts, the photocatalytic efficiency of the available ternary chalcogenide heterojunctions is still low, thus they cannot be utilized in practical applications. For high photocatalytic efficiency and practical applications, it is still essential to fabricate more efficient ternary chalcogenide heterojunctions. Our experimental results suggested the more negative conduction band of AgInS₂ (−0.41 V) than that of SnIn₄S₈ (−0.24 V) and the more positive valence band of SnIn₄S₈ (+1.51 V) than that of AgInS₂ (+1.28 V), which make it possible to fabricate SnIn₄S₈/AgInS₂ heterojunction for efficient charge separation and enhanced photocatalytic activity.

In this work, we developed a novel heterojunction photocatalyst by coupling AgInS₂ with SnIn₄S₈ (AgInS₂/SnIn₄S₈, abbreviated as AIS/SIS) via one-step hydrothermal method. The molar ratio of SnIn₄S₈ to AgInS₂ has an obvious effect on charge separation and photocatalytic activity of SnIn₄S₈/AgInS₂ heterojunction under visible-light irradiation. A synergistic effect and proper bandgap match between AgIn₅S₈ and AgInS₂ play important roles in the high photocatalytic performance of SnIn₄S₈/AgInS₂ heterojunction. SnIn₄S₈/AgInS₂ heterojunction shows high photocatalytic degradation performance for 2NP and TC-HCl solution. Moreover, 20 mg AgInS₂/SnIn₄S₈ heterojunction can effectively treat 100 mL real pharmaceutical industry wastewater in presence of H₂O₂ with 65.98% mineralization efficiency, and the chemical oxygen demand (COD) of real pharmaceutical industry wastewater decreases to 153 mg/L, which meets the discharge standards of industrial effluent.

2. Experimental section

2.1. Chemicals

Thioacetamide (TAA, AR) and indium trichloride tetrahydrate (InCl₃·4H₂O, 99.99%) were purchased from Sinopharm Group Chemical Reagent Co., Ltd. Silver nitrate (AgNO₃), tin tetrachloride pentahydrate (SnCl₄·5H₂O, AR), anhydrous ethanol (C₂H₅OH, AR), anhydrous sodium sulfate (Na₂SO₄, AR), sodium hydroxide (NaOH, AR), triethanolamine (TEOA) and isopropanol (IPA) were obtained from Shantou Xilong Chemical Co., Ltd. (Shantou, China). Tetracycline hydrochloride (TC-HCl) and 2-nitrophenol (2NP) were acquired from Shanghai Aladdin Biochemical Technology Co., Ltd (Shanghai, China). *p*-Benzoquinone (BQ) was obtained from Beijing Bailingwei Technology Co., Ltd. (Beijing, China).

2.2. Synthesis of AgInS₂/SnIn₄S₈

AgInS₂/SnIn₄S₈ nanosheet heterojunctions were synthesized via a simple one-pot hydrothermal method. AgNO₃ and SnCl₄·5H₂O were dissolved in 30 mL deionized water, then thioacetamide was added to the above solution under magnetic stirring for 30 min until solid was completely dissolved. Finally, the solution was transferred to 50 mL Teflon-lined autoclave. The sealed autoclave was heated at 180 °C for 12 h, then cooled to room temperature naturally. The products were washed with deionized water and absolute ethanol for several times, and finally dried at 60 °C for 12 h. Samples with 0.2:1, 0.4:1, 0.6:1, 0.8:1 and 1:1 molar ratio of AgInS₂ to SnIn₄S₈ were denoted as (0.2:1)AIS/SIS, (0.4:1)AIS/SIS, (0.6:1)AIS/SIS, (0.8:1)AIS/SIS and (1:1)AIS/SIS, respectively.

2.3. Characterization

The crystal structure of AgInS₂/SnIn₄S₈ was determined by X-ray diffractometer (XRD). The morphologies of AgInS₂/SnIn₄S₈ were taken on a scanning electron microscopy (SEM) instrument (Shimadzu, Japan) and transmission electron microscopy (TEM, JEOL, Japan). The elemental analysis was conducted by energy dispersive spectrometry (EDS, Shimadzu, Japan). UV-vis diffuse reflectance spectra (DRS) of AgInS₂/SnIn₄S₈ samples were measured by U-3900H spectrophotometer (Hitachi, Japan). The specific surface area and pore structure measurements were carried out by a GEMINI VII 2390 surface area and porosity analyzer (Micromeritics, USA). The photoluminescence (PL) emission spectra were obtained by a fluorescence spectrometer (HITACHI F-7000). Total organic carbon (TOC) of 2NP solution and pharmaceutical industry wastewater was determined using an Apollo 9000 TOC analyzer (Terkmar-Dohrmann, USA).

2.4. Electrochemical measurement

Electrochemical and photoelectrochemical measurements were performed in a three-electrode system. The three-electrode system was composed of graphite electrode as counter electrode, saturated calomel electrode (SCE) as reference electrode, and ITO glass coated with AgInS₂/SnIn₄S₈ as working electrode, and a 300 W xenon lamp (PLS-SXE300, Beijing Trusttech Co., Ltd., China) with a 420 nm cut off filter was served as visible-light source.

The flat-band potential and semiconductor type of AgInS₂/SnIn₄S₈ can be determined by Mott-schottky curves. Mott-schottky plots were performed in three-electrode system with scan frequency of 1000 Hz and potential range of −1.0–1.0 V using 0.5 mol/L Na₂SO₄ electrolyte solution. Photocurrent experiment was similar to Mott-schottky test with the applied voltage of 0 V for the ITO working electrode. Electrochemical impedance spectroscopy (EIS) was determined at an AC voltage magnitude of 0 mV with the frequency range of 10⁵–1 Hz, and the electrolyte solution was the mixture of 2.5 mmol/L potassium hexacyanoferrate (III) (K₃[Fe(CN)₆]), and 2.5 mmol/L potassium ferrocyanide (K₄[Fe(CN)₆]).

2.5. Evaluation of photocatalytic activity

Photocatalytic activities of AgInS₂/SnIn₄S₈ were evaluated by degrading 2NP and TC-HCl under visible-light irradiation. 20 mg AgInS₂/SnIn₄S₈ photocatalysts was added in a 100 mL 10 mg/L of 2NP and TC-HCl solution, respectively. Before the irradiation, the suspension was magnetically stirred for 120 min in the dark to ensure adsorption-desorption equilibrium. The concentration of 2NP and TC-HCl at adsorption-desorption equilibrium was recorded as C₀. 3 mL suspension was sampled intermittently during visible-light irradiation and immediately filtered by 0.25 μm membrane filter. The clear solution was measured by Hitachi U-3900H UV-vis spectrophotometer and TOC-VCPh total organic carbon analyzer. The effect of pH on the photocatalytic degradation performance of AgInS₂/SnIn₄S₈ was studied by adjusting solution pH with NaOH or HCl solution.

2.6. Active species trapping experiments

To detect the active species during photocatalytic reaction, IPA, BQ, and TEOA were used as hydroxyl radical (OH[•]) scavenger, superoxide radical (O₂^{•-}) scavenger and hole (h⁺) scavenger, respectively. The quenchers were added in the photocatalytic system of AgInS₂/SnIn₄S₈ for 2NP degradation.

2.7. The practical application of $\text{AgInS}_2/\text{SnIn}_4\text{S}_8$ in real pharmaceutical industry wastewater

The sampling process for the mineralization and COD removal of real pharmaceutical industry wastewater was similar to that of photocatalytic activity measurement. The TOC of filtrate was analyzed using a TOC-VCPH total organic carbon analyzer. The COD of filtrate was measured according to the standard method [31].

3. Results and discussion

3.1. XRD analysis

Fig. 1 shows the XRD patterns of AIS, SIS and AIS/SIS heterojunctions with different molar ratio. It can be seen that AIS shows characteristic peaks at 23.17° , 27.29° , 33.23° , 43.57° and 47.62° , which corresponds to (220), (311), (400), (511) and (440) planes of AgInS_2 (PDF#26-1477). The diffraction peaks at 2θ of 27.5° , 28.7° , 33.3° , 43.7° , 47.8° and 60.78° were observed for SIS, corresponding to (311), (222), (400), (333), (440) and (444) indices of tetragonal phase SnIn_4S_8 (PDF#42-1305). The characteristic peaks position of pure SnIn_4S_8 is very close to that of pure AgInS_2 , and thus characteristic peaks position of SnIn_4S_8 are coincident with that of AgInS_2 in the XRD patterns of AIS/SIS heterojunctions, indicating strong chemical interaction between AgInS_2 and SnIn_4S_8 .

3.2. SEM and EDS analysis

Fig. 2 shows the SEM images of AIS, SIS and (0.6:1)AIS/SIS heterojunction at different magnification. Pure AIS was composed of numerous interlaced nanosheets with thickness of about 5 nm, and pure SIS shows various small block aggregations of particles with irregular shapes. In case of (0.6:1)AIS/SIS heterojunctions, the

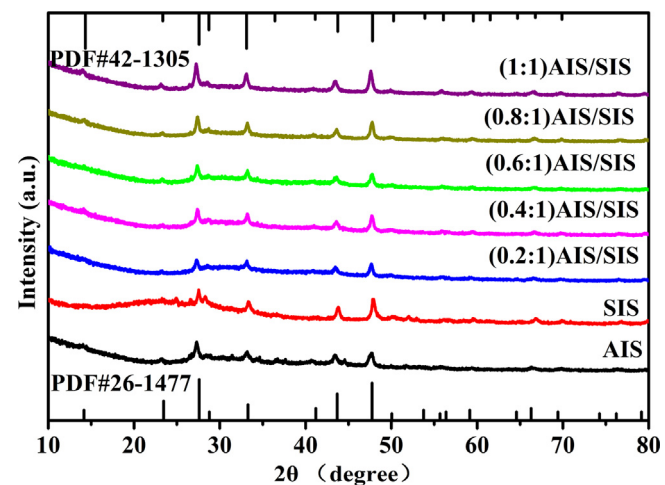


Fig. 1. XRD patterns of pure AIS, pure SIS and AIS/SIS heterojunctions with different molar ratio.

thickness of nanosheets is about 15–20 nm, and stacked together to form large aggregates.

The EDS spectrum of (0.6:1)AIS/SIS was shown in **Fig. 3**. It can be seen from **Fig. 3** that the elements of Ag, Sn, In and S were observed and atomic percentage of Ag, Sn, In and S is 7.23%, 7.24%, 29.48% and 56.06%, respectively.

3.3. TEM and high-resolution TEM

The microstructure of AIS, SIS and (0.6:1)AIS/SIS heterojunction was further investigated by TEM and high-resolution TEM (**Fig. 4**). The TEM images of AIS, SIS and (0.6:1)AIS/SIS heterojunction con-

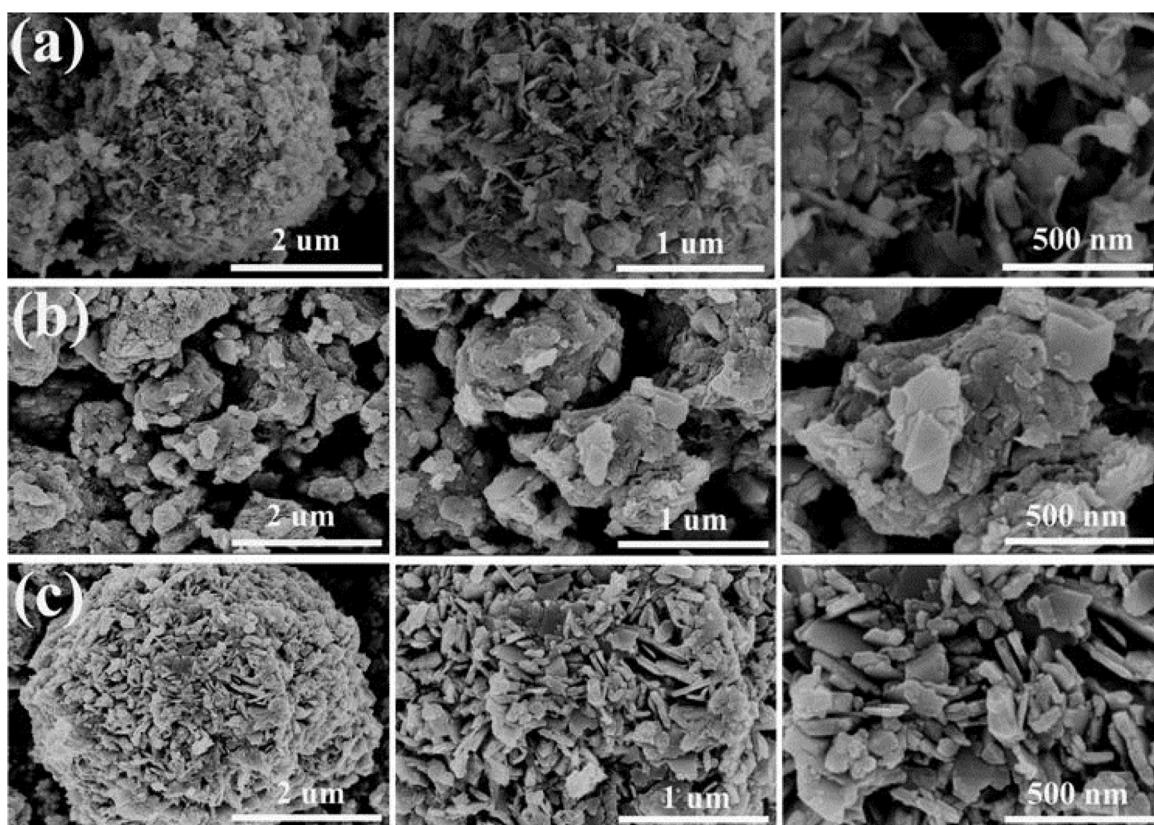


Fig. 2. SEM images of (a) pure AIS, (b) pure SIS, and (c) (0.6:1)AIS/SIS heterojunctions.

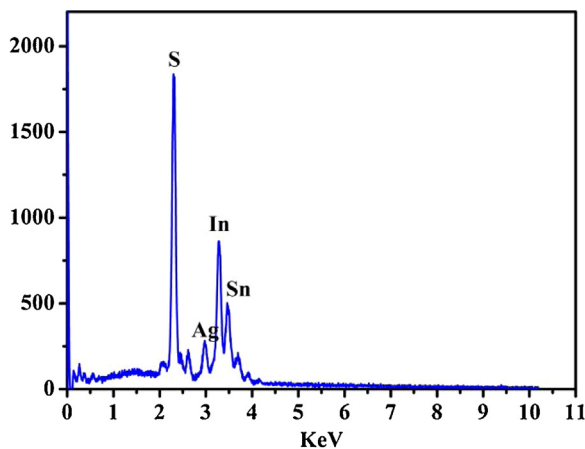


Fig. 3. EDS spectrum of (0.6:1)AIS/SIS.

firmed the aggregation of nanosheets. The lattice fringe of 0.379 nm in the high-resolution TEM of AIS depict (220) plane of AgInS₂ (Fig. 4d). The high-resolution TEM of SIS showed two sets of different lattice fringes with fringe spacing of 0.625 nm and 0.323 nm, corresponding to the (111) and (220) facets of SnIn₄S₈, respectively. The measured d spacings of 0.622 and 0.380 nm in the (0.6:1)AIS/SIS heterojunction correspond to the (111) crystal planes of SnIn₄S₈ and (220) crystal planes of AgInS₂, respectively.

3.4. BET surface areas and pore structure

Fig. 5 displays the nitrogen adsorption-desorption isotherms and the corresponding pore size distribution curves of AIS, SIS and AIS/SIS heterojunctions with different molar ratio. As shown in Fig. 5a, the isotherms of all the samples were identified as type IV with H₃ hysteresis loop, suggesting the formation of slit-like pores resulted from aggregation of nanosheets, which is in conformity with SEM results. The pore size distribution is mainly in the range of 3~10 nm (Fig. 5b). The specific surface area, pore volume and average pore size of AIS, SIS and AIS/SIS heterojunctions with different molar ratio were summarized in Table 1, and the results confirm their mesoporous structure.

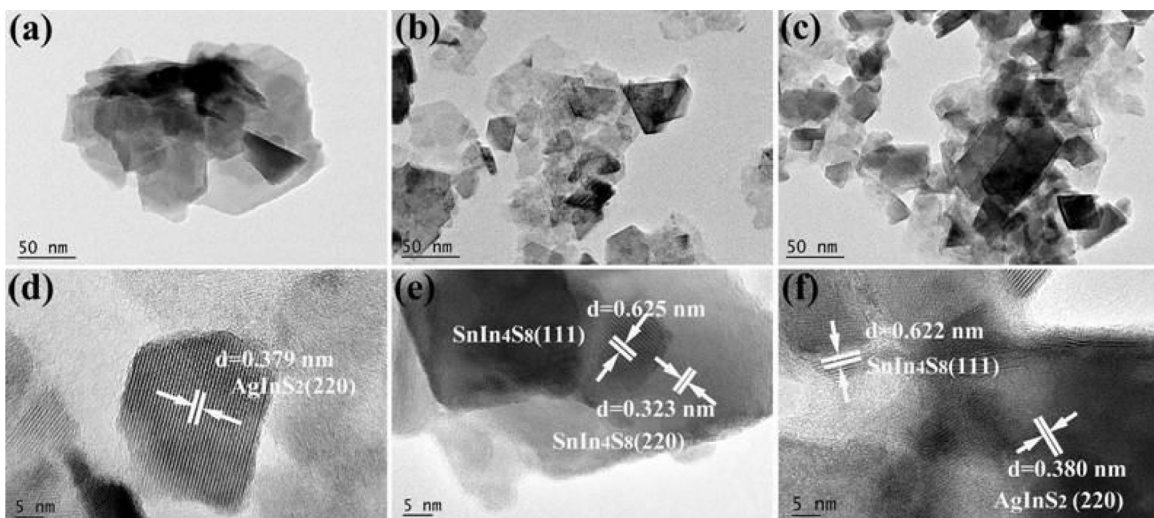


Fig. 4. TEM images of (a) pure AIS, (b) pure SIS, and (c) (0.6:1)AIS/SIS heterojunctions and HRTEM images of (d) pure AIS, (e) pure SIS and (f) (0.6:1)AIS/SIS heterojunctions.

Table 1
Physical properties of pure AIS, SIS and AIS/SIS heterojunctions.

Samples	S_{BET} ($\text{m}^2 \text{g}^{-1}$)	Pore volume ($\text{cm}^3 \text{g}^{-1}$)	Average pore size (nm)
AIS	11.7	0.056	19.3
SIS	10.3	0.035	13.5
(0.2:1)AIS/SIS	4.9	0.011	8.9
(0.4:1)AIS/SIS	33.7	0.062	7.4
(0.6:1)AIS/SIS	36.3	0.075	8.2
(0.8:1)AIS/SIS	21.7	0.046	8.1
(1:1)AIS/SIS	7.4	0.021	9.6

Table 2

The band gap energies (E_g), flat-band potential (E_{fb}), conduction band (E_{CB}) and valence band (E_{VB}) position of pure AIS, SIS and AIS/SIS heterojunctions.

Samples	E_g (eV)	V_{fb} (V vs. SCE)	E_{CB} (V vs. NHE)	E_{VB} (V)
AIS	1.69	-0.34	-0.41	1.28
SIS	1.75	-0.38	-0.24	1.51
(0.2:1)AIS/SIS	1.86	-0.42	-0.31	1.55
(0.4:1)AIS/SIS	1.79	-0.46	-0.37	1.42
(0.6:1)AIS/SIS	1.65	-0.61	0.43	1.22
(0.8:1)AIS/SIS	1.77	-0.67	-0.38	1.39
(1:1)AIS/SIS	1.81	-0.49	-0.40	1.41

3.5. UV-vis diffuse reflectance spectra

Fig. 6 depicts the UV-vis diffuse reflectance spectra of AIS, SIS and AIS/SIS heterojunctions. The AIS, SIS and AIS/SIS heterojunctions show strong absorption in the visible-light region. The band gap (E_g) of AIS, SIS and AIS/SIS heterojunctions can be calculated from the following formula:

$$\alpha h\nu = A(h\nu - E_g)^{n/2}$$

where α , h , ν and A represent the absorption coefficient, Planck's constant, light frequency and a constant, respectively. The band gap energies (E_g) of the samples can be evaluated by extrapolating the plots of $(\alpha h\nu)^2$ versus $h\nu$ to $(\alpha h\nu)^2 = 0$ (Fig. 6b), and the values of band gap energies were summarized in Table 2.

3.6. PL analysis

In order to further investigate the recombination probability of photogenerated electrons and holes, the photoluminescence properties of the materials were studied at excitation wavelength of 310 nm (Fig. 7). The PL intensity of AIS/SIS heterojunctions is lower

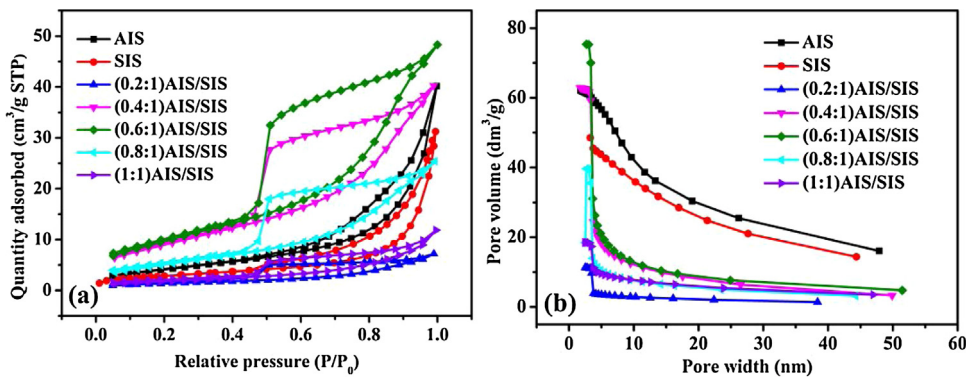


Fig. 5. (a) Nitrogen adsorption-desorption isotherms and (b) the corresponding pore-size distribution curves of pure AIS, pure SIS and AIS/SIS heterojunctions with different molar ratio.

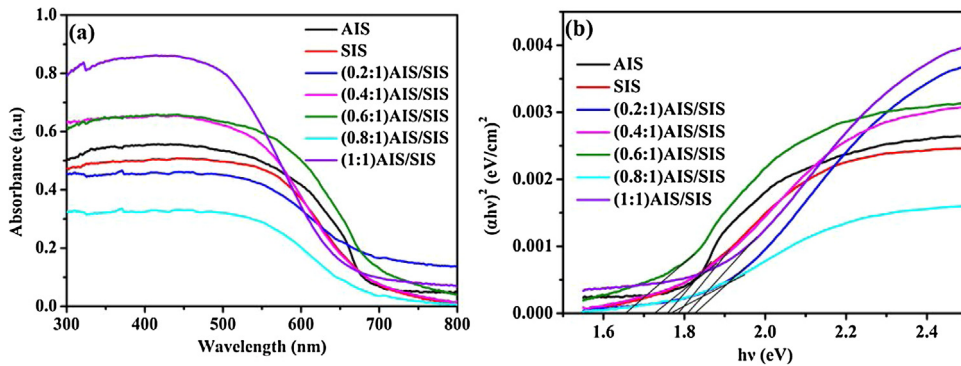


Fig. 6. (a) UV-vis diffuse reflectance spectra of pure AIS, pure SIS and AIS/SIS heterojunctions, (b) Plots of $(ahv)^2$ versus hv of pure AIS, pure SIS and AIS/SIS heterojunctions.

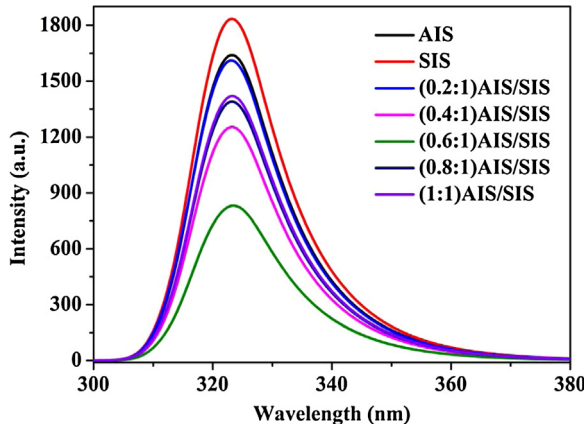


Fig. 7. PL spectra of pure AIS, pure SIS and AIS/SIS heterojunctions.

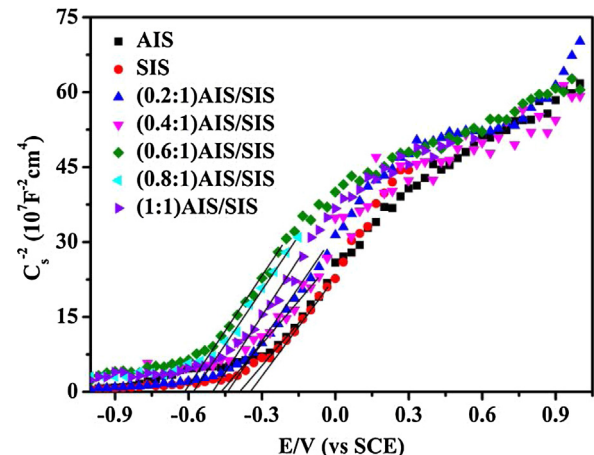


Fig. 8. Mott-Schottky curves of pure AIS, pure SIS and AIS/SIS heterojunctions.

3.7. Photoelectrochemical measurements

than that of pure AIS and pure SIS, indicating that more efficient charge separation of AIS/SIS heterojunctions than pure AIS and pure SIS, and the coupling of SIS with AIS can inhibit or retard recombination of the photo-generated carriers. Moreover, the PL intensity of AIS/SIS heterojunctions is remarkably insensitive to the ratio of AIS to SIS. With the molar ratio of AIS to SIS increasing from 0.2 to 0.6, the PL intensity of AIS/SIS heterojunctions decreases, and the fluorescence intensity is the minimum in case of (0.6:1)AIS/SIS, implying the most efficient separation of photogenerated electrons and holes. However, further increasing the AIS:SIS proportion leads to the enhancement of PL intensity.

The flat band potential (V_{fb}) of AIS, SIS and AIS/SIS heterojunctions can be evaluated by extrapolating the linear part of the Mott-Schottky plot to $\frac{1}{C^2} = 0$ (Fig. 8):

$$\frac{1}{C^2} = \frac{2}{A^2 e \epsilon \epsilon_0 N_A} \left(E - V_{fb} - \frac{k_B T}{e} \right)$$

where C , E , ϵ_0 , ϵ , T , e , k_B , N_A and V_{fb} correspond to interfacial capacitance, applied potential, dielectric constant of the semiconductor, permittivity of free space, absolute temperature, electronic charge, Boltzmann constant, carrier concentration and flat band potential, respectively. The positive slope of the linear part indicated *n*-type

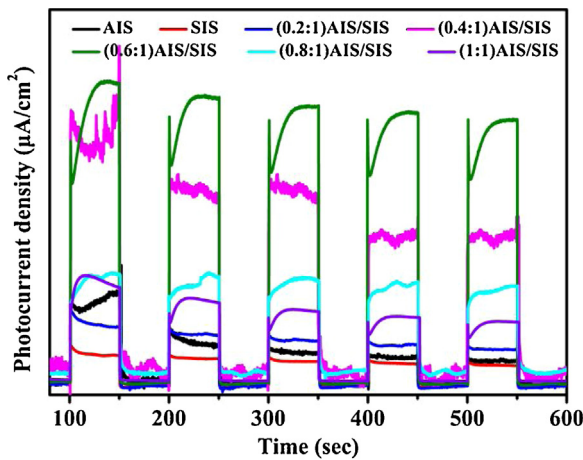


Fig. 9. Photocurrent responses of pure AIS, pure SIS and AIS/SIS heterojunctions.

semiconductor characteristics of pure AIS, pure SIS and AIS/SIS heterojunctions, and the flat band potential values of all the samples were listed in Table 2.

To further reveal the separation of photogenerated charge carriers, the photocurrent response of pure AIS, pure SIS and AIS/SIS heterojunctions with different molar ratio was carried out during repeated on-off cycles of visible-light irradiation without the bias potential (Fig. 9). Pure pure AIS, pure SIS and AIS/SIS exhibit reproducible photocurrent response without obvious decay. The photocurrent density decreases in the following order: (0.6:1)AIS/SIS > (0.4:1)AIS/SIS > (0.8:1)AIS/SIS > (1:1)AIS/SIS > (0.2:1)AIS/SIS > pure AIS > pure SIS. The photocurrent values of pure AIS and pure SIS anode are about $6.41 \mu\text{A}\text{cm}^{-2}$ and $5.24 \mu\text{A}\text{cm}^{-2}$, respectively. The photocurrent intensity of (0.6:1)AIS/SIS heterojunction is maximum with value of $59.48 \mu\text{A}\text{cm}^{-2}$, indicating that the coupling of SnIn_4S_8 with AgInS_2 with proper molar ratio can effectively suppress charge recombination and improve charge separation efficiency [32,33].

The electrochemical impedance spectra of pure AIS, pure SIS and AIS/SIS heterojunctions were shown in Fig. 10. The diameter of the semicircular Nyquist plots increases the following order: (0.6:1)AIS/SIS < (0.4:1)AIS/SIS < (0.8:1)AIS/SIS < (1:1)AIS/SIS < (0.2:1)AIS/SIS < pure AIS < pure SIS, which is consistent with the order of PL intensity and contrary to the photocurrent order, further confirming the more efficient charge separation by coupling AIS with SIS and the synergic effect between AIS and SIS [34].

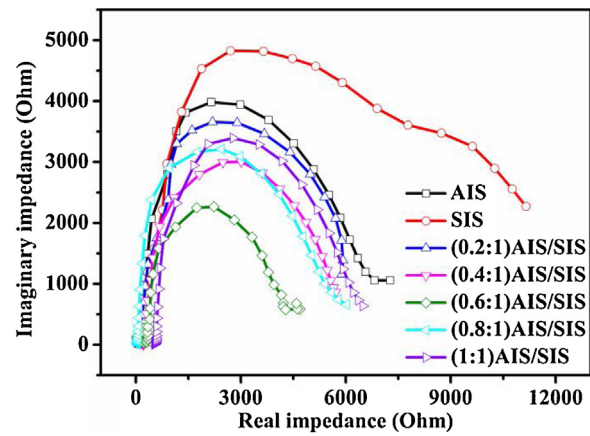


Fig. 10. Electrochemical impedance spectroscopy of pure AIS, pure SIS and AIS/SIS heterojunctions.

3.8. Adsorption capacity and photocatalytic activity

3.8.1. Adsorption kinetics and photocatalytic degradation of 2NP

Adsorption kinetics can influences subsequent photocatalytic process, thus the adsorption kinetics of 2NP on AIS, SIS and (0.6:1)AIS/SIS was investigated (Fig. S1). The adsorption equilibrium of 2NP on AIS, SIS and (0.6:1)AIS/SIS is 4.33, 9.91 and 8.11 mg/g, respectively. Moreover, the adsorption kinetics of 2NP on pure AgInS_2 , SnIn_4S_8 and $\text{AgInS}_2/\text{SnIn}_4\text{S}_8$ heterojunction follow the pseudo-second-order model (Fig. S2, Table S1). These results indicated that the adsorption of 2NP on pure AgInS_2 , pure SnIn_4S_8 and $\text{AgInS}_2/\text{SnIn}_4\text{S}_8$ heterojunction is not an important factor to remove 2NP, and following photocatalytic degradation is a primary process for removing 2NP.

The visible-light photocatalytic performance of pure AIS, pure SIS and AIS/SIS heterojunctions was assessed by degrading 10 mg/L 2NP (Fig. 11). The degradation efficiency of 2NP by pure AIS, pure SIS, (0.2:1)AIS/SIS, (0.4:1)AIS/SIS, (0.6:1)AIS/SIS, (0.8:1)AIS/SIS and (1:1)AIS/SIS heterojunctions are 52%, 50%, 73%, 89%, 92%, 78% and 76% respectively. The photocatalytic activities of AIS/SIS heterojunctions are much higher than those of pure AIS and pure SIS, and the photocatalytic activities of AIS/SIS heterojunctions are consistent with their photocurrent order.

The photocatalytic activities of pure AIS, pure SIS and (0.6:1)AIS/SIS are obviously influenced by solution pH (Fig. 11b). When solution pH increases in the range of 1.0–5.0, the photocatalytic activities of pure AIS, pure SIS and (0.6:1)AIS/SIS increase dramatically, and exhibits the highest photocatalytic activities at

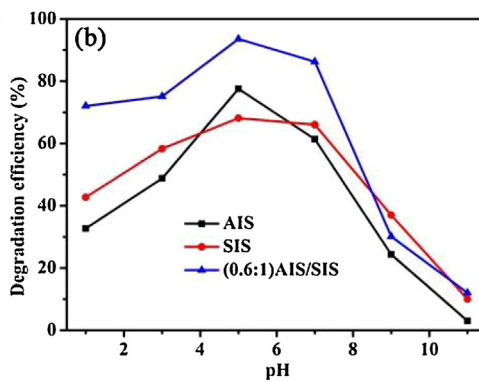
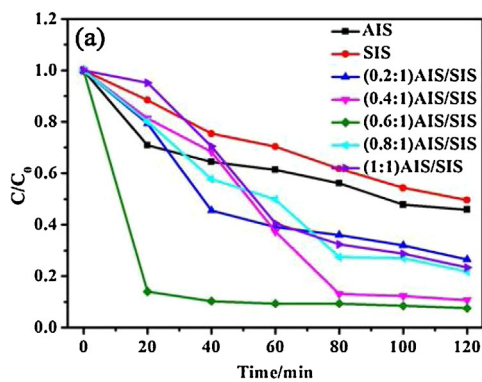


Fig. 11. (a) Photocatalytic degradation of 2NP by pure AIS, pure SIS and AIS/SIS heterojunctions, (b) The effect of solution pH on photocatalytic degradation of 2NP in the presence of pure AIS, pure SIS and AIS/SIS heterojunctions.

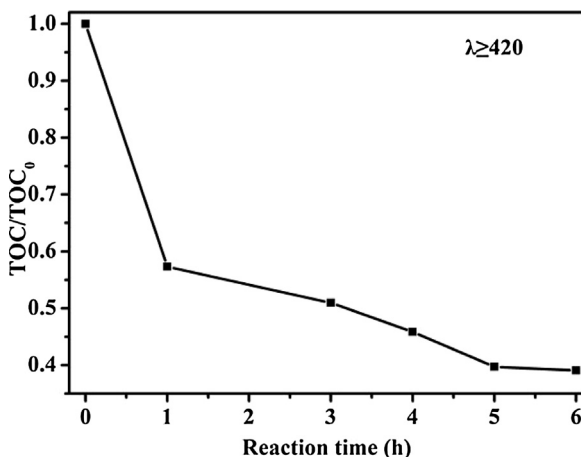


Fig. 12. TOC change of 2NP solution by (0.6:1)AIS/SIS heterojunction.

pH 5.0, while there is a sharp decrease in the photocatalytic activities with further increasing solution pH from 5.0 to 11. The solution pH-dependent photocatalytic activities may be related with the surface charge of photocatalysts and the different forms of 2NP at different pH.

In order to explore the mineralization degree of 2NP, TOC removal of 2NP by (0.6:1)AIS/SIS heterojunctions under visible-light irradiation was investigated (Fig. 12). The COD removal efficiency of 2NP is 60.93% within 6 h under visible-light illumination, indicating that most of 2NP can be fully mineralized to CO_2 and water in the degradation process.

3.8.2. The adsorption and visible-light photocatalytic degradation of TC-HCl

In order to confirm photocatalytic performance of pure AIS, pure SIS and (0.6:1)AIS/SIS heterojunctions for degrading other organic pollutants, the adsorption and photocatalytic degradation of TC-HCl by pure AIS, pure SIS and (0.6:1)AIS/SIS heterojunctions were explored (Fig. 13). The adsorption efficiency of TC-HCl over pure AIS, pure SIS, (0.2:1)AIS/SIS, (0.4:1)AIS/SIS, (0.6:1)AIS/SIS, (0.8:1)AIS/SIS and (1:1)AIS/SIS composites was 7.45%, 76.71%, 73.09%, 56.09%, 37.26%, 5.14% and 77.17%, respectively. The results indicated that adsorption of TC-HCl on these photocatalysts is considerable, and adsorption plays an important role in removing TC-HCl. In order to further investigate the photocatalytic activity of AIS/SIS heterojunctions, the photocatalytic performance of (0.7:1)AIS/SIS, (0.75:1)AIS/SIS, (0.85:1)AIS/SIS and (0.9:1)AIS/SIS for degrading TC-HCl was studied (Fig. 13b). From the results we can infer that the molar ratio of AIS to SIS between 0.75 and 0.9 is advantageous

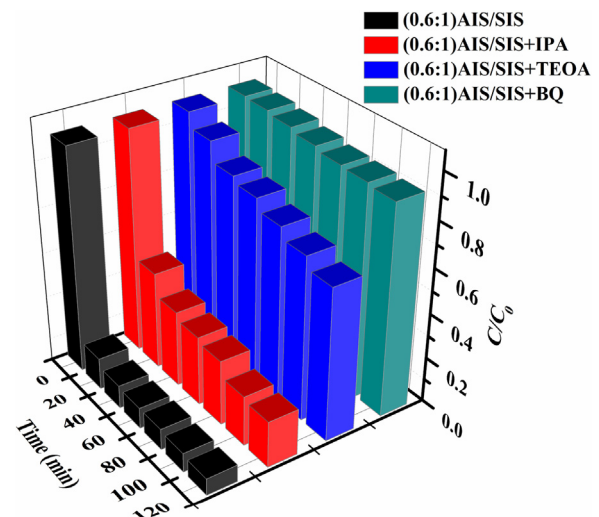


Fig. 14. Active species trapping experiment of (0.6:1)AIS/SIS.

for photocatalysis. The results illustrated that adsorption and photocatalysis play synergistic roles in effective removal of TC-HCl.

3.9. Photocatalytic mechanism

To reveal the main active species during the photocatalytic degradation process, free radicals trapping experiments were carried out (Fig. 14). In case of no quencher in the photocatalytic system, the degradation efficiency of 2NP was 92%. The addition of TEOA (holes scavenger) and BQ ($\bullet\text{O}_2^-$ quencher) can greatly suppress the photocatalytic activity of AIS/SIS for degrading 2NP, and degradation efficiency of 2NP decreases to 33% and 7%, respectively. When IPA ($\bullet\text{OH}$ quencher) was added, there is no obvious decrease in degradation efficiency of 2NP. The results imply that $\bullet\text{O}_2^-$ and holes play major role in photocatalytic degradation process, but $\bullet\text{OH}$ radicals are not the main active species.

Based on main active species trapping experiments, band gap energy, and the position of valence band and conduction band, the photocatalytic mechanism of $\text{AgInS}_2/\text{SnIn}_4\text{S}_8$ heterojunction was illustrated in Scheme 1. Under visible-light irradiation, the electrons in the VB of AgInS_2 and SnIn_4S_8 can be excited to their CB, and synchronously leave behind equal amounts of holes in their VB, thus forming the electron–hole pairs. The photogenerated electrons (e^-) can be transferred from conduction band (CB) of AgInS_2 to SnIn_4S_8 , and holes (h^+) can be transferred from the valence band (VB) of SnIn_4S_8 to AgInS_2 , which hinders the recombination of the electron and holes [35–37]. The adsorbed O_2 on the surface can interact with photogenerated e^- to form $\bullet\text{O}_2^-$ radicals. Because the

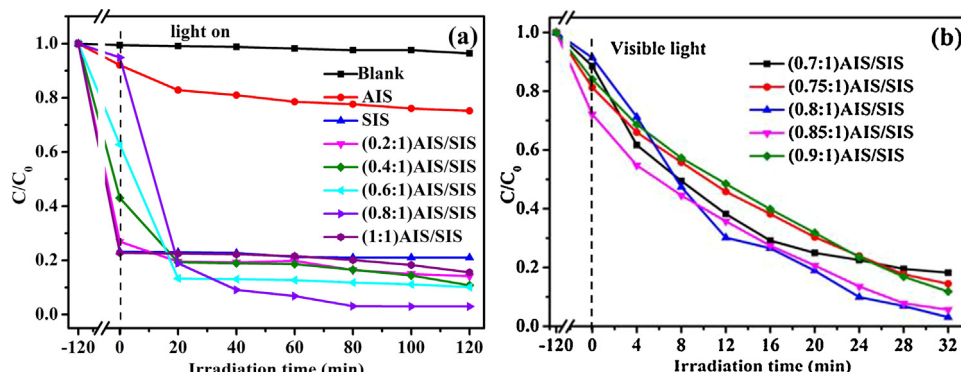


Fig. 13. Adsorption and photocatalytic degradation of TC-HCl by pure AIS, pure SIS and AIS/SIS heterojunctions.

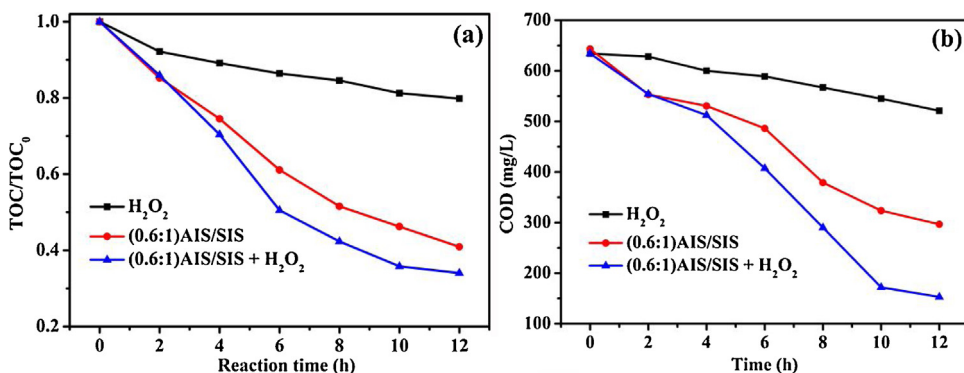
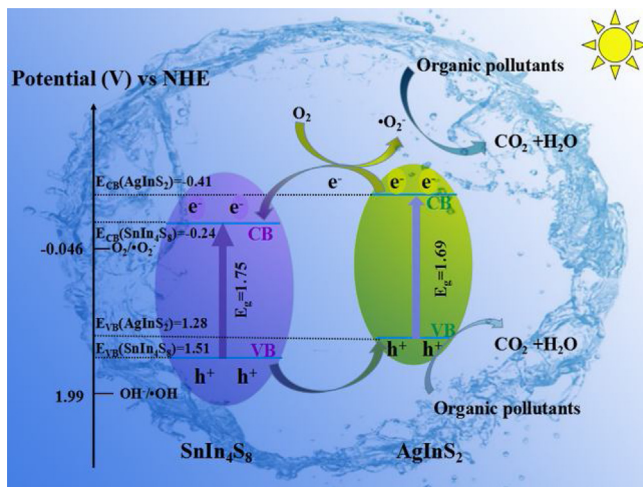


Fig. 15. (a) The mineralization efficiency of pharmaceutical wastewater, and (b) The COD removal of real pharmaceutical wastewater by (0.6:1)AIS/SIS heterojunction.



Scheme 1. Possible photocatalytic mechanism of AIS/SIS heterojunctions.

valence band (VB) of AgInS₂ and AgIn₄S₈ is lower than the standard redox potential of •OH/OH⁻ (+1.99 V vs. NHE), the photogenerated holes cannot oxidize hydroxyl ion (OH⁻) to form •OH. The •O₂⁻ radicals together with the photo-generated holes can directly oxidize organic pollutants.

3.10. The practical application of AIS/SIS in real pharmaceutical industry wastewater

Although AIS/SIS exhibits good adsorption or photocatalytic performance for the removal of 2NP and tetracycline, whether it can effectively treat real wastewater is still unknown due to the complicated components and hydrochemical condition of real wastewater. Thus the mineralization efficiency and COD removal of pharmaceutical industry wastewater (100 mL) from Jiangxi Chemedir Biopharm-tech. Co., Ltd. (Jiujiang, China) under visible-light irradiation was investigated by adding 20 mg (0.6:1)AIS/SIS (Fig. 15). When 5 mL H₂O₂ (30%) was added, the mineralization efficiency of pharmaceutical industry wastewater is only 20.18%. The mineralization efficiency of pharmaceutical industry wastewater is 59.09% in presence of (0.6:1)AIS/SIS, and the mineralization efficiency can increase to 65.98% in presence of both 20 mg (0.6:1)AIS/SIS and 5 mL H₂O₂, indicating AIS/SIS play an important part in the mineralization of pharmaceutical industry wastewater, and H₂O₂ can promote the mineralization process.

The initial COD of pharmaceutical wastewater is 634 mg/L. The COD of pharmaceutical wastewater decreases to 521 and 296.7 mg/L with adding 5 mL 30% H₂O₂ and 20 mg (0.6:1)AIS/SIS, respectively. In case of both (0.6:1)AIS/SIS and H₂O₂ in the sys-

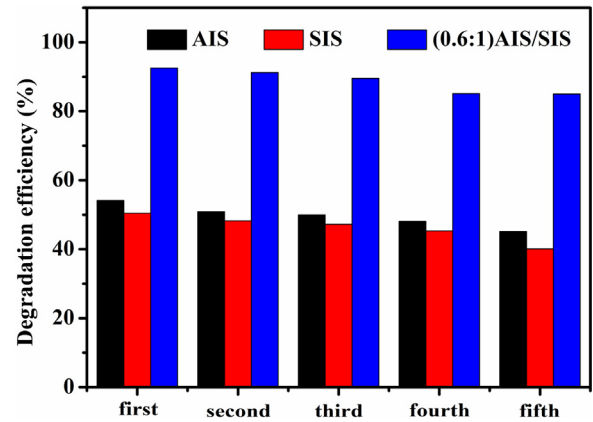


Fig. 16. The reusability of (0.6:1)AIS/SIS heterojunction.

tem, the COD of pharmaceutical wastewater decreases to 153 mg/L, which meets the discharge standards of industrial effluent.

3.11. Recyclability and photostability of AIS/SIS

The stability of pure AIS, pure SIS and (0.6:1)AIS/SIS heterojunctions was evaluated for five consecutive photocatalytic degradation cycles (Fig. 16). The degradation efficiency of 2NP on fresh AIS, SIS and (0.6:1)AIS/SIS is 54.12%, 50.45% and 92.52%, respectively. After five repeated use without using regeneration means, the degradation efficiency of 2NP on reused AIS, SIS and AIS/SIS decreases to 45.12%, 40.12% and 85.12%, respectively. The above results indicated that (0.6:1)AIS/SIS shows high photocatalytic activity and can maintain long-term activity without obvious deactivation due to strong chemical interaction between AIS and SIS, whereas pure AIS and pure SIS show relatively low photocatalytic performance and there is almost 10% loss in photocatalytic activity after five catalytic cycles.

XRD comparison of the fresh and reused (0.6:1)AIS/SIS heterojunction catalysts shows that there is no change of crystal structure and no other impurity peaks appear in photocatalytic degradation-regeneration cycles (Fig. S3, Supporting Information), indicating that AIS/SIS is still stable after the photocatalytic degradation reaction.

The surface elemental composition and chemical states of the fresh and reused (0.6:1)AIS/SIS were further analyzed by XPS (Fig. 17). The survey XPS spectra show that the fresh and recycled (0.6:1)AIS/SIS heterojunctions not only contain Ag, Sn, In and S elements, but only contain C and O elements which result from the organic sulfur precursor and the contamination. Moreover, there is no obvious change in the XPS of AgInS₂/SnIn₄S₈ heterojunc-

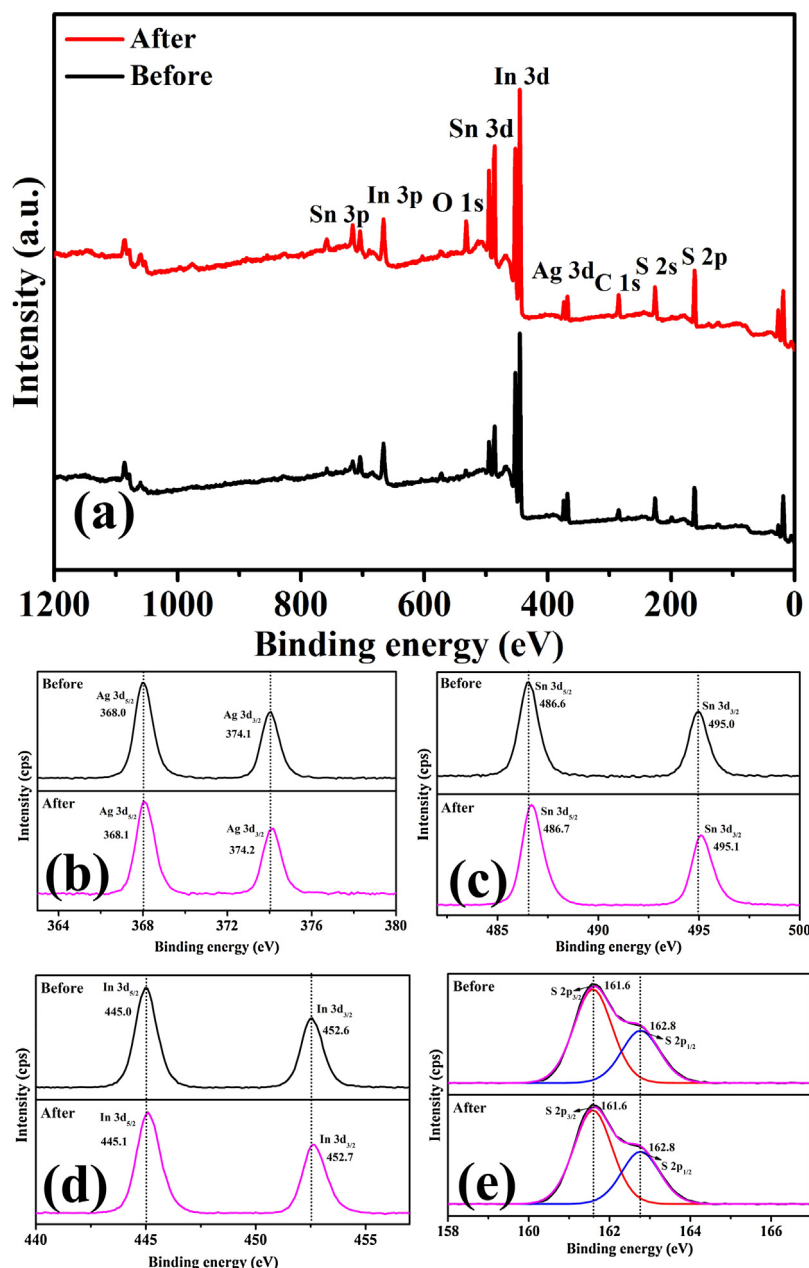


Fig. 17. XPS comparison of the fresh and reused (0.6:1) AIS/SIS.

tion after five cycles, indicating the high stability and reusability of $\text{AgInS}_2/\text{SnIn}_4\text{S}_8$ photocatalysts.

4. Conclusions

A series of $\text{AgInS}_2/\text{SnIn}_4\text{S}_8$ nanosheet heterojunctions were successfully fabricated using one-pot hydrothermal strategy. The as-prepared $\text{AgInS}_2/\text{SnIn}_4\text{S}_8$ heterojunctions with suitable molar ratio exhibit extraordinary high visible-light photocatalytic degradation performance and stability. The high photocatalytic activity of $\text{AgInS}_2/\text{SnIn}_4\text{S}_8$ heterojunction is attributed to the efficient charge separation, and its high catalytic stability after five consecutive catalytic cycles without using regeneration means could be attributed to strong chemical interaction between AgInS_2 and SnIn_4S_8 . Moreover, $\text{AgInS}_2/\text{SnIn}_4\text{S}_8$ heterojunctions can treat real pharmaceutical wastewater efficiently to meet the emission standards.

Acknowledgment

This work was supported by Natural Science Foundation of China (51308278, 51178213, 51238002), Department of Education Fund of Jiangxi Province (GJJ150742), Natural Science Foundation of Jiangxi Province (2016BAB206117), Science Fund for Excellent Young Scholars of Jiangxi Province (20162BCB23038).

Appendix A. Supplementary data

Supplementary data associated with this article can be found, in the online version, at <http://dx.doi.org/10.1016/j.apcatb.2017.07.051>.

References

- [1] S. Miralles-Cuevas, I. Oller, A. Agüera, M. Llorca, J.A. Sánchez Pérez, S. Malato, *J. Hazard. Mater.* 323 (2017) 442–451.

- [2] X. Zhang, C. Chen, P. Lin, A. Hou, Z. Niu, J. Wang, *Environ. Sci. Technol.* 45 (2011) 161–167.
- [3] R.P. Schwarzenbach, T. Egli, T.B. Hofstetter, U.V. Gunten, B. Wehrli, *Annu. Rev. Env. Resour.* 35 (2010) 109–136.
- [4] W. Wu, C. Jiang, V.A. Roy, *Nanoscale* 7 (2014) 38–58.
- [5] G. Darabdhara, P.K. Boruah, P. Borthakur, N. Hussain, M.R. Das, T. Ahamad, S.M. Alshehri, V. Malgras, K.C. Wu, Y. Yamauchi, *Nanoscale* 8 (2016) 8276–8287.
- [6] H. Cheng, B. Huang, Y. Dai, *Nanoscale* 6 (2014) 2009–2026.
- [7] Y. Wang, Q. Wang, X. Zhan, F. Wang, M. Saifdar, J. He, *Nanoscale* 5 (2013) 8326–8339.
- [8] X. Yang, W. Chen, J. Huang, Y. Zhou, Y. Zhu, C. Li, *Nature* 5 (2015) 10632.
- [9] H. Zhang, L.H. Guo, D. Wang, L. Zhao, B. Wan, *ACS Appl. Mater. Interfaces* 7 (2015) 1816–1823.
- [10] X. Luo, F. Deng, L. Min, S. Luo, B. Guo, G. Zeng, C. Au, *Environ. Sci. Technol.* 47 (2013) 7404–7412.
- [11] M. Niu, D. Cheng, D. Cao, *Nature* 4 (2014) 4810.
- [12] T. Leijtens, G.E. Eperon, S. Pathak, A. Abate, M.M. Lee, H.J. Snaith, *Nat. Commun.* 4 (2013) 2885.
- [13] Y.C. Zhang, L. Yao, G.S. Zhang, D.D. Dionysiou, J. Li, X.H. Du, *Appl. Catal. B: Environ.* 144 (2014) 730–738.
- [14] Y.C. Zhang, Q. Zhang, Q.W. Shi, Z.Y. Cai, Z.J. Yang, *Sep. Purif. Technol.* 142 (2015) 251–257.
- [15] Y.C. Zhang, M. Yang, G.S. Zhang, Dionysiou D. Dionysiou, *Appl. Catal. B: Environ.* 142–(143) (2013) 249–258.
- [16] L. Wang, X. Li, W. Teng, Q. Zhao, Y. Shi, R. Yue, Y. Chen, *J. Hazard. Mater.* 244–245 (2013) 681–688.
- [17] S.K. Batabyal, S.E. Lu, J.J. Vittal, *Cryst. Growth Des.* 16 (2016) 2231–2238.
- [18] S. Jeong, H.C. Yoon, N.S. Han, H.O. Ji, S.M. Park, B.K. Min, Y.R. Do, J.K. Song, *J. Phys. Chem. C* 121 (2017) 3149–3155.
- [19] S. Shen, L. Li, Z. Wu, M. Sun, Z. Tang, J. Yang, *RSC Adv.* 7 (2017) 4555–4562.
- [20] T. Yan, L. Li, G. Li, Y. Wang, W. Hu, X. Guan, *J. Hazard. Mater.* 186 (2011) 272–279.
- [21] F. Deng, F. Zhong, P. Hu, X. Pei, X. Luo, S. Luo, *J. Nanopart. Res.* 19 (2017) 14–27.
- [22] B. Mao, C.H. Chuang, J. Wang, C. Burda, *J. Phys. Chem. C* 115 (2011) 8945–8954.
- [23] T. Yan, L. Li, G. Li, *Res. Chem. Intermediat.* 37 (2011) 297–307.
- [24] Y. Hamanaka, T. Ogawa, M. Tsuzuki, T. Kuzuya, *J. Phys. Chem. C* 115 (2011) 1786–1792.
- [25] Z. Chen, W. Wang, Z. Zhang, X. Fang, *J. Phys. Chem. C* 117 (2017) 19346–19352.
- [26] S. Shenawikhalil, V. Uvarov, S. Fronton, I. Popov, Y. Sasson, *J. Phys. Chem. C* 116 (2012) 11004–11012.
- [27] Y. Yu, Y. Tang, J. Yuan, Q. Wu, W. Zheng, Y. Cao, *J. Phys. Chem. C* 118 (2014) 13545–13551.
- [28] K. Li, B. Chai, T. Peng, J. Mao, L. Zan, *ACS Catal.* 3 (2013) 170–177.
- [29] T. Wang, Y. Zhang, T. Ding, *Mater. Lett.* 123 (2014) 153–155.
- [30] B. Liu, X. Li, Q. Zhao, J. Ke, M. Tadé, S. Liu, *Appl. Catal. B: Environ.* 185 (2016) 1–10.
- [31] A.D. Eaton, L.S. Clesceri, A.E. Greenberg, M.A.H. Franson, A.D. Eathion, M. Franson, L.S. Clesceri, A.S. Greenberg, J. Connors, D. Jenkis, *Standard Methods for the Examination of Water and Wastewater*, American Public Health Association, 1995.
- [32] Y.C. Zhang, F. Zhang, Z.J. Yang, H.G. Xue, D.D. Dionysiou, *J. Catal.* 344 (2016) 692–700.
- [33] F. Zhang, Y.C. Zhang, C.Q. Zhou, Z.J. Yang, H.G. Xue, D.D. Dionysiou, *Chem. Eng. J.* 324 (2017) 140–153.
- [34] F. Zhang, T. Ding, Y.C. Zhang, Z.J. Yang, H.G. Xue, *Mater. Lett.* 192 (2017) 149–152.
- [35] Z.Y. Zhang, J.D. Huang, Y.R. Fang, M.Y. Zhang, K.C. Liu, B. Dong, *Adv. Mater.* 29 (18) (2017) 1606688–1606696.
- [36] Z.Y. Zhang, Y.Z. Huang, K.C. Liu, L.J. Guo, Q. Yuan, B. Dong, *Adv. Mater.* 27 (2015) 5906–5914.
- [37] Z.Y. Zhang, K.C. Liu, Z.Q. Feng, Y.N. Bao, B. Dong, *Sci. Rep.* 6 (2016) 19221–19230.